PCCP

PAPER

View Article Online
View Journal

Cite this: DOI: 10.1039/c5cp00266d

Electrical conductivity and thermopower of $(1 - x)$ $BiFeO_3$ – $xBi_{0.5}K_{0.5}TiO_3$ (x = 0.1, 0.2) ceramics near the ferroelectric to paraelectric phase transition

E. T. Wefring, M.-A. Einarsrud and T. Grande*

Received 16th January 2015,
Accepted 2nd March 2015

DOI: 10.1039/c5cp00266d

www.rsc.org/pccp

Ferroelectric $BiFeO_3$ has attractive properties such as high strain and polarization, but a wide range of applications of bulk $BiFeO_3$ are hindered due to high leakage currents and a high coercive electric field. Here, we report on the thermal behaviour of the electrical conductivity and thermopower of $BiFeO_3$ substituted with 10 and 20 mol% $Bi_{0.5}K_{0.5}TiO_3$. A change from p-type to n-type conductivity in these semi-conducting materials was demonstrated by the change in the sign of the Seebeck coefficient and the change in the slope of the isothermal conductivity *versus* partial pressure of O. A minimum in the isothermal conductivity was observed at $\sim 10^{-2}$ bar O_2 partial pressure for both solid solutions. The strong dependence of the conductivity on the partial pressure of O_2 was rationalized by a point defect model describing qualitatively the conductivity involving oxidation/reduction of Fe^{3+}, the dominating oxidation state of Fe in stoichiometric $BiFeO_3$. The ferroelectric to paraelectric phase transition of 80 and 90 mol% $BiFeO_3$ was observed at 648 ± 15 and 723 ± 15 °C respectively by differential thermal analysis and confirmed by dielectric spectroscopy and high temperature powder X-ray diffraction.

1. Introduction

Legislations, prohibiting the use of lead in electronics, have been passed by the European Union and other countries due to environmental concerns.[1,2] Lead-free piezoelectric materials have therefore received significant interest in recent years to replace the state of the art lead-containing piezoelectric $Pb(Zr,Ti)O_3$ (PZT).[2] Bismuth containing perovskite-based materials are among the most promising lead-free alternatives, and among these bismuth ferrite, $BiFeO_3$ (BFO), and bismuth potassium titanate, $Bi_{0.5}K_{0.5}TiO_3$ (BKT), have been investigated intensively.[2,3] BFO with a rhombohedral structure has attracted tremendous interest due to its multiferroic properties,[3,4] including the potential as a ferro- or piezoelectric material with high polarization, lattice strain and Curie temperature (T_C, 830 °C), the latter being important for high temperature applications.[5–7] The prospects of applying BFO are though hampered by parasitic secondary phases formed during synthesis,[8,9] and a high coercive electric field and high dielectric losses stemming from conductivity.[3,10] BKT is a tetragonal ferroelectric which shows a relatively high piezoelectric constant and T_C (380 °C).[11,12] Challenges with the fabrication of dense BKT ceramics have been reported[13] but dense single phase materials can be obtained by solid state synthesis.[14] BKT is also an important constituent in solid solution systems, which may possess a morphotropic phase boundary (MPB) similar to the one known for PZT.[2]

Solid solutions of BFO and BKT have recently been investigated due to a possible MPB.[12,13,15–20] Solid solutions of BFO with BKT suppresses the formation of the parasitic phases well known in pure BFO and phase pure BFO–BKT materials are obtain by conventional solid state synthesis.[8,15] BFO–BKT materials are isostructural with BFO at a high BFO content. A maximum in the dielectric and electromechanical properties is reported at 25 mol% BFO, and the piezoelectric properties such as electric field induced polarization and strain decreases towards a high BFO content.[15,17] This is probably due to the high coercive electric field and dielectric loss of BFO relative to that of BKT.[5,13] Morozov *et al.* have recently shown that the conductivity of BFO–BKT materials can be reduced by annealing in an inert atmosphere improving the electromechanical performance.[20] A Maxwell–Wagner type relaxation in BFO–BKT, coupled to the electrical conductivity and point defects, has also been reported.[21]

One of the main challenges with to BFO is the high electrical conductivity giving rise to dielectric loss.[3] Pure and acceptor substituted BFO shows the characteristics of p-type conductivity in air, relating conductivity to the presence of Fe^{4+}.[22–26] The conductivity of 0.7BFO–0.3BKT can be manipulated by thermal treatment in an oxidizing or an inert atmosphere.[20,21] The aliovalent

Department of Materials Science and Engineering, Norwegian University of Science and Technology, Trondheim, 7491 Trondheim, Norway. E-mail: grande@ntnu.no

substitution of Fe^{3+} with *e.g.* Ti^{4+} and Ni^{2+} on the perovskite B site has profound effect on the conductivity of BFO[27–29] where tetravalent cations reduce the conductivity and divalent cations increase the conductivity. Particularly, substitution with Ti has shown great promise to reduce the conductivity of BFO.[27,29,30] The observed effects are discussed in relation to the presence of Fe^{2+} and oxygen vacancies, and coulometric titration has shown that 2 mol% Fe^{2+} can be present in BFO before decomposition of BFO occurs under reducing conditions.[31] However, the effect of the presence of Fe^{2+} on the conductivity of bulk BFO has yet to be established.

Evaporation of Bi_2O_3 during synthesis increases the point defect concentration in BFO materials.[10] Bi vacancies can be charge compensated by oxygen vacancies or oxidation of Fe^{3+}. The presence of multivalent Fe will strongly influence the electrical conductivity of BFO, as it depends on small polaron hopping.[27,28,32] P-type (in air) and n-type (reducing conditions) semiconductor behaviour has previously been reported for several related Fe-containing perovskites, including $La_{1-x}Sr_xFeO_{3-\delta}$[33–35] and $LnFeO_3$ (Ln = Pr, Nd, Sm, Eu and Gd).[36,37] In these materials the electronic conductivity is strongly linked to polaron hopping and the oxidation state of Fe, which is strongly dependent on the partial pressure of oxygen ($p(O_2)$).

Here we report on the electrical conductivity and thermopower of BFO substituted with 10 and 20 mol% BKT. This solid solution was chosen as the model system to obtain physical insight into the electrical conductivity of BFO-based materials, avoiding the influence of secondary phases typically found in pure bulk BFO. We provide experimental evidence for the change of the conductivity from p-type to n-type when going from oxidizing to inert conditions, demonstrating clearly for the first time why the electrical conductivity can be minimized by annealing at controlled partial pressure of oxygen. The ferroelectric phase transition of the materials is investigated by high temperature X-ray diffraction, dielectric spectroscopy/electrical conductivity and differential thermal analysis. Finally, a conventional point defect model is applied to describe the dependence of the electrical conductivity on $p(O_2)$.

2. Experimental

Ceramics with composition $(1 - x)$ $BiFeO_3$ – $xBi_{0.5}K_{0.5}TiO_3$ (x = 0.2, 0.1, denoted 0.8BFO and 0.9BFO) were prepared by solid state synthesis as reported by Morozov *et al.*[17] Stoichiometric amounts of dried Bi_2O_3 (Aldrich, 99.9% or 99,99%), K_2CO_3 (Aldrich, 99.99%), TiO_2 (Aldrich, 99.9% or 99,99%) and Fe_2O_3 (Aldrich, 99.999%) precursors were mixed and ball milled in isopropanol (18 h). The precursor mixture was calcined (5 h) in air at 820 °C (x = 0.2) and 800 °C (x = 0.1). The calcined powders were ball milled in isopropanol (18 h), dried and sieved (250 μm sieve), and further pressed into pellets/bars by uniaxial pressing and cold isostatic pressing (200 MPa). The samples were sintered in air (2 h) covered by a sacrificial powder at 1010 °C (x = 0.2) and 980 °C (x = 0.1). Powders for X-ray diffraction (XRD) were prepared by crushing the sintered pellets followed by annealing the powders above the Curie temperature.

The density of the materials was measured by the Archimedes method (ISO 5017:1998(E)) and the relative density was calculated with respect to the crystallographic density determined by XRD. The grain size was determined by the intercept method from polished and thermally etched samples (880 °C, 5 min) using a scanning electron microscope (SEM; Hitachi S-3400N).

Electronic conductivity was measured using a direct current (DC) four-point method, as previously described by Wærnhus *et al.*[38] The surface of sintered bars was ground using a grade #220 silicon carbide grinding paper to dimensions of about 22 × 4.5 × 3 mm. A constant voltage was applied over the current circuit and the distance between the voltage electrodes on the sample was 5 mm. Pt-paste was used to ensure sufficient contact between the current electrodes and the sample. The DC electrical conductivity was measured at 700, 750 and 800 °C at a constant $p(O_2)$. The temperature was reduced to 650 °C before a new $p(O_2)$ was introduced. The conductivity relaxation was observed and the conductivity was allowed to stabilize under the specific conditions before the temperature or the atmosphere was altered. The temperature was measured by using an S-type thermocouple and the partial pressure of oxygen (O_2, 0.2, 0.02, 0.002, N_2) was controlled by mixing O_2 and N_2 (Yara Praxair, 5.0) at flow rates of 50, 250 or 500 mL min^{-1}.

The Seebeck-coefficient (Q) was measured at 650, 700, 750 and 800 °C using a ProboStat™ setup (NorECs AS) in a vertical tubular furnace with a vertical bar analogous to the bar used to measure the electrical conductivity. The temperature gradient was measured by two S-type thermocouples (20–25 °C) and the voltage across the sample was measured using Pt-electrodes. The atmosphere was varied by manual flow control of O_2, N_2 and synthetic air (Yara Praxair, 5.0).

Dielectric properties were investigated in synthetic air (Yara Praxair, 5.0) using a frequency analyzer (Alpha-A High Performance Frequency Analyser, Novocontrol Technologies) connected to a ProboStat™ setup in a vertical tubular furnace. Gold electrodes were sputtered onto ground and cleaned faces of a sintered pellet, and measurements were performed during continuous heating/cooling (2 °C min^{-1}) every 30 second at frequencies 1–10^6 Hz. The electroded sample was first heated/cooled to/from 400 °C to remove Maxwell–Wagner contributions to the permittivity.[21] The reported data are obtained from the 2nd heating cycle to 720 °C and 800 °C for 0.8BFO and 0.9BFO, respectively.

High temperature X-ray diffraction (HTXRD) was performed using a θ–θ Bruker D8 ADVANCE diffractometer utilizing Cu K_α radiation and a VANTEC-1 position sensitive detector. Powders for investigation were contained within an alumina sample holder and heated using a radiant heater mounted within an MRI Physikalische Geräte GmbH high temperature camera. Calibration of the system against an Al_2O_3 standard gave an estimated temperature error of ±15 °C. Diffraction patterns were collected from room temperature to 760 °C (every 50 degrees up to 510 °C, every 10 degrees above 510 °C), across an angular range 20–75° 2θ with a step size of 0.016° (1 second/step).

Lattice parameters for each diffraction pattern were determined by Pawley fitting using the Topas software.[39] A hexagonal model (*R3c*) was adopted below the Curie temperature and a cubic model ($Pm\bar{3}m$) above, as previously described for $BiFeO_3$ and Mn-doped $BiFeO_3$.[40,41] Peak shapes were described using a Pseudo-Voigt model (TCHZ) and a Chebychev polynomial background function was used. Sample displacement and lattice parameters were refined for each temperature.

Differential thermal analysis (DTA) was used to determine the ferroelectric to paraelectric phase transition (STA 449 C, Netzsch). The powder used for DTA was prepared the same way as the powder for XRD, from the same sintered pellet. The powder was packed in alumina crucibles and heated to 750 °C (0.8BFO) and 800 °C (0.9BFO) at 10 °C min^{-1} in synthetic air (30 mL min^{-1}). The samples were kept at T_{max} for 5 minutes before cooling.

3. Results

Dense (97 ± 1% of theoretical density) and phase pure ceramics with compositions 0.8BFO and 0.9BFO were successfully prepared by conventional solid state synthesis. No secondary phases could be observed in the sintered specimens by X-ray diffraction in agreement with previous work.[17] The microstructure of the dense and single phase materials, shown in Fig. 1, is relatively homogeneous with the submicron grain size (Table 1). No evidence for the presence of any secondary phases could be observed by SEM/back scattered electrons. The room temperature unit cell parameters determined from the diffraction pattern (not shown) are given in Table 1.

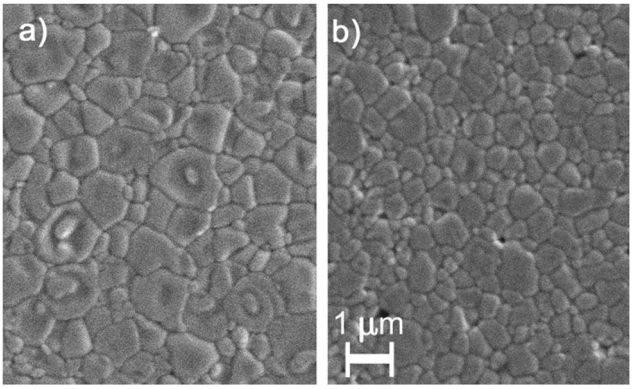

Fig. 1 SEM micrographs (secondary electrons) of polished and thermally etched 0.8BFO (a) and 0.9BFO (b) ceramics.

The DC electrical conductivity of 0.8BFO and 0.9BFO is shown as a function of temperature and $p(O_2)$ in Fig. 2a and b, respectively. The conductivity increases with increasing BFO content, reflecting a higher conductivity of BFO relative to BKT,[42,43] and it increases with increasing temperature in line with a semiconductor behaviour. A distinct minimum in the isothermal conductivity *versus* $\log p(O_2)$, typical for the p-type to n-type transition of oxide semiconductors, is evident for both compositions. P-type conductivity is characteristic for the materials in oxidizing atmosphere, while n-type is typical for inert or reducing conditions. A similar p-type behaviour is observed for Ca-substituted, $BiFeO_3$,[26] but the minimum in the conductivity as well as the n-type conductivity in bulk BFO-materials has not been reported previously.

While the materials were single phase after sintering, it is worth noting that an Fe/Ti-rich secondary phase was observed on the surface of the materials after a long period of electrical DC conductivity measurement (640 and 770 hours for 0.8BFO and 0.9BFO respectively). The formation of the secondary phase on the surface is most likely related to the loss of Bi_2O_3 during the measurements as shown previously for pure BFO.[4]

The Seebeck coefficients in the temperature range 650–800 °C in three different atmospheres, shown in Fig. 3, demonstrate clearly the p-type conductivity in air and oxygen and n-type conductivity in an inert atmosphere. The negative Seebeck coefficient is to the author's knowledge the first direct evidence for n-type conductivity of bulk BFO-rich materials. The positive Seebeck coefficient for BFO at 650 °C in air has been reported as ~600 μV K^{-1} in reasonable agreement with the present data. It is clear that the Seebeck coefficient increases with increasing BKT content.[43]

The real part of the permittivity of 0.8BFO during heating (10 kHz, 100 kHz, 1 MHz) and cooling (10 kHz) in synthetic air is shown in Fig. 4a. No temperature dispersion of the maximum

Table 1 Lattice parameters, grain size and phase transition temperature of 0.8BFO and 0.9BFO

		0.8BFO	0.9BFO
Room temperature lattice parameters	*a* [Å]	5.591(8)	5.584(6)
	c [Å]	13.80(6)	13.840(8)
Grain size	[μm]	0.9 ± 0.05	0.6 ± 0.03
Permittivity heating	Temp. of perm. max [°C] 10 kHz	675 ± 15	—
Permittivity cooling		620 ± 15	—
Phase transition HTXRD	[°C]	630 ± 15	676 ± 15
DTA heating	Peak onset [°C]	648 ± 15	723 ± 10
	Peak max [°C]	680 ± 1	746 ± 1
DTA cooling	Peak onset [°C]	641 ± 5	743 ± 10
	Peak min [°C]	619 ± 1	713 ± 1

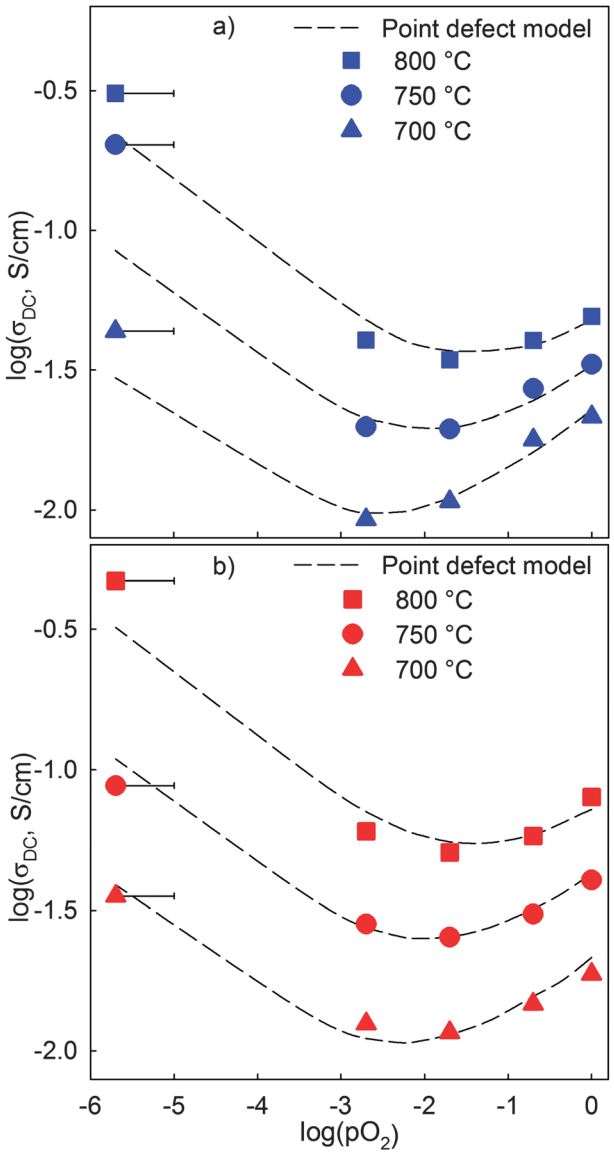

Fig. 2 DC conductivity of 0.8BFO (a) and 0.9BFO (b) as a function of $p(O_2)$ at 700, 750 and 800 °C. The dashed lines are the conductivity calculated by the point defect model introduced in the discussion section. The uncertainty associated with the $p(O_2)$ in N_2 is shown by error bars.

permittivity (ε'_{max}) is observed during heating, pointing to a true ferroelectric phase transition in line with what is previously reported.[21] The temperature of ε'_{max} is included in Table 1. The shift in the maximum permittivity observed during cooling points to a first order phase transition. Permittivity data for 0.9BFO are not reported due to the high conductivity of this particular material close to the phase transition.

The real part of the AC conductivity (10 kHz) during heating is shown for 0.8BFO and 0.9BFO in Fig. 4b. The conductivity increases with temperature and changes slope around 240 °C and in the temperature range of the ferroelectric to paraelectric phase transition for all frequencies. The DC conductivity measured during heating is in good accordance with the data measured under isothermal conditions (Fig. 2).

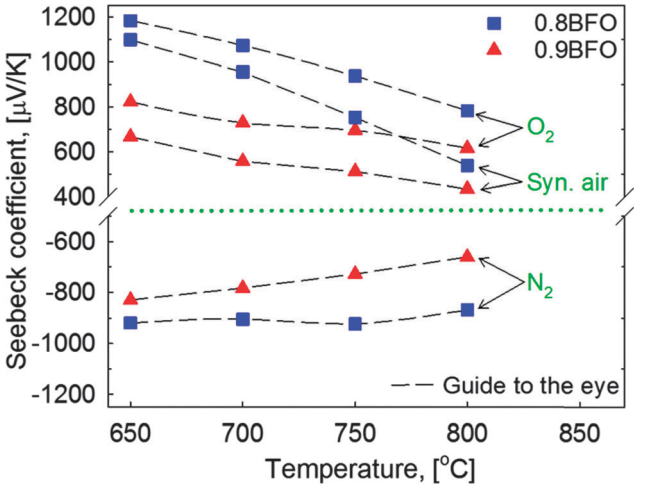

Fig. 3 The Seebeck coefficient of 0.8BFO and 0.9BFO as a function of temperature in three different atmospheres.

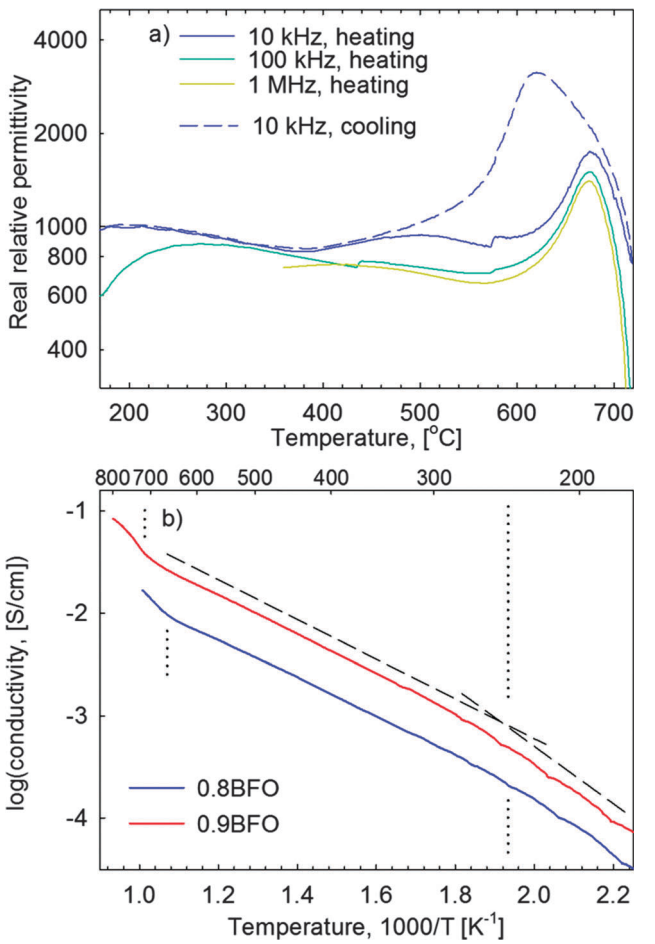

Fig. 4 The real permittivity during heating (solid lines) and cooling (dashed line) of 0.8BFO (a) and the real part of the AC conductivity (10 kHz) for 0.8BFO and 0.9BFO during heating (b). In (b), the dashed lines show the slope and dotted lines mark temperature ranges of the changing slope. All measurements were performed in synthetic air.

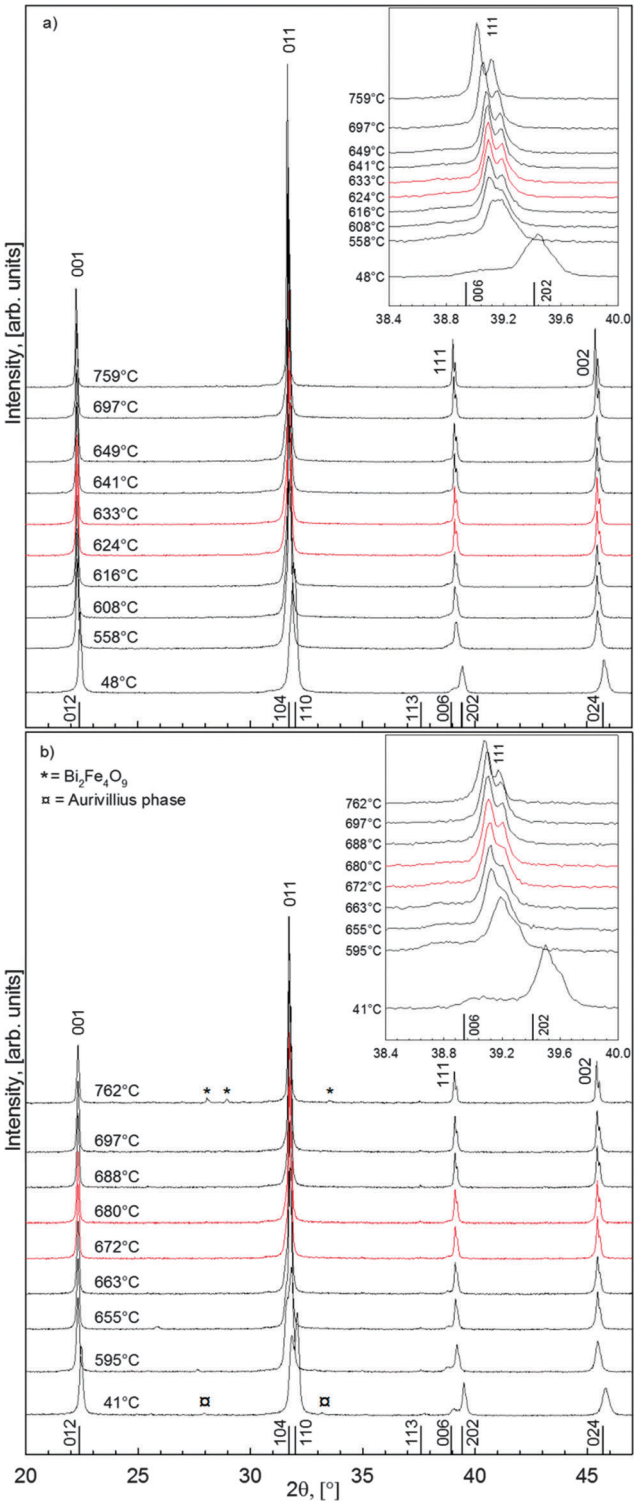

Fig. 5 X-ray diffractograms of 0.8BFO (a) and 0.9BFO (b) at selected temperatures. The vertical bars show the reflections with indices for rhombohedral BFO. The Miller indices above the reflections refer to the cubic symmetry at a high temperature. The phase transition occurs in the temperature range of the red diffractograms (624 and 633 °C for 0.8BFO, 672 and 680 °C for 0.9BFO). The inset shows the 006/202 diffraction lines in detail. The secondary phase (¤) seen at low temperature in 0.9BFO was not present after sintering, but appeared after thermal annealing above T_C prior to the HTXRD analysis.

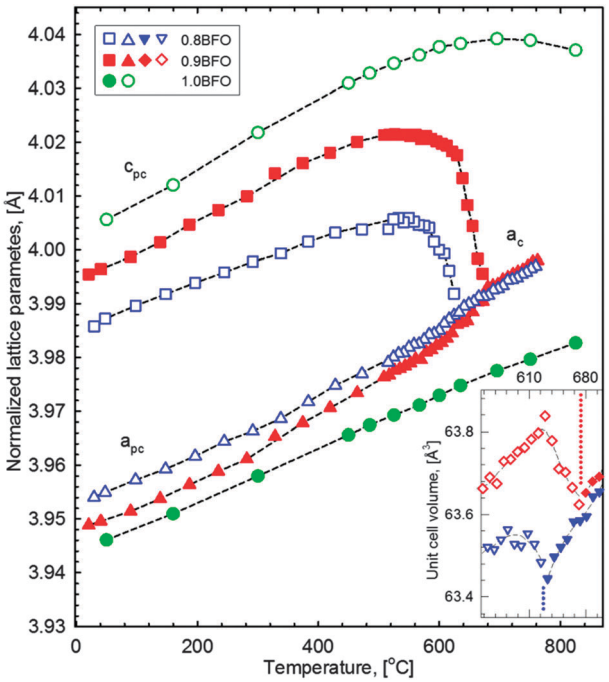

Fig. 6 Refined and pseudo cubic (normalized) lattice parameters for 0.8BFO, 0.9BFO and BFO (1.0BFO).[45] Dashed lines serve as a guide to the eye. The inset shows unit cell volume below (open symbols) and above (filled symbols) the ferroelectric phase transition (marked by dotted lines).

The thermal evolution of the HTXRD diffractograms of 0.8BFO and 0.9BFO is shown in Fig. 5a and b, respectively. Both materials were indexed to the *R3c* space group from room temperature up to the ferroelectric to paraelectric phase transition temperature. The most pronounced change with temperature is the reduced splitting of the (006) and (202) reflections (inset in Fig. 5a and b). Above the phase transition the diffraction patterns were indexed using the space group $Pm\bar{3}m$. Pure BFO is known to be orthorhombic *Pbnm* above T_C,[44] but no super reflections due to tilting of the octahedra could be observed and the cubic space group was therefore used. The phase transition temperatures were estimated to be 630 ± 15 °C (0.8BFO) and 676 ± 15 °C (0.9BFO) based on the diffraction data (Table 1).

The thermal evolution of the pseudo cubic unit cell parameters for 0.9BFO and 0.8BFO is compared to the lattice parameters of pure BFO in Fig. 6.[45] The unit cell parameters are normalized as follows: $a_{pc} = 2^{-1/2}\ a_h$ and $c_{pc} = 12^{-1/2}\ c_h$, where pc and h refer to pseudo cubic and hexagonal, respectively. The thermal expansion of a_{pc} and c_{pc} is close to linear far below the phase transition. A strong contraction of the *c*-axis is evident close to T_C as reported for $BiFeO_3$ due to the ferroelectric to paraelectric phase transition.[44,45] The unit cell volume is discontinuous at the phase transition (inset Fig. 6) demonstrating a 1st order phase transition as reported for BFO.[44,45]

The phase transition of 0.8BFO and 0.9BFO observed by DTA is presented in Fig. 7. An endothermic peak upon heating and an exothermic peak during cooling are clearly evident.

The temperature for the onset of the peaks is included in Table 1 along with the temperature of the peak maximum/minimum. The hysteresis between the heating and cooling curves confirms the 1st order of the phase transition.

4. Discussion

The qualitative behaviour of the electrical conductivity at different $p(O_2)$ for 0.8BFO and 0.9BFO shows great similarities to the properties reported for similar Fe-based perovskite materials.[33–37] The electrical conductivity of these materials has previously been modelled with success by a mass action type treatment of point defect equilibria. A mass action type model adapted for 0.8BFO and 0.9BFO is introduced here based on the approach presented by Mizusaki *et al.*[35] for $LaFeO_3$. The substitution of K^+ into the A-site and Ti^{4+} into the B-site of BFO can be seen as acceptor and donor substitution, respectively, resulting in K'_{Bi} and $Ti^{\bullet}_{Fe}$ as point defects using the Kröger-Vink notation. These two point defects are charge balanced by the K : Ti substitution ratio of 1 : 2, and can therefore be neglected for a first approximation. The point defect chemistry in $(1-x)$BFO–xBKT can, analogous to $LaFeO_3$, be described by a model based on 5 equations. First, the point defect equilibria related to the volatility of Bi_2O_3 (1), the principle of electro neutrality (2) and the mass balance of Fe (3), are defined.

$$2Bi^{\times}_{Bi} + 3O^{\times}_{O} \rightarrow 2V'''_{Bi} + 3V^{\bullet\bullet}_{O} + 2Bi(g) + \frac{3}{2}O_2(g) \quad (1)$$

$$p + 2\left[V^{\bullet\bullet}_{O}\right] = n + 3\left[V'''_{Bi}\right] \quad (2)$$

$$\left[Fe_{Fe}\right] = n + \left[Fe^{\times}_{Fe}\right] + p \quad (3)$$

Here, V'''_{Bi} is Bi vacancy, $V^{\bullet\bullet}_{O}$ is an oxygen vacancy and n and p are concentrations of electrons and holes, respectively. The electrons and holes correspond to the concentration of Fe^{2+} and Fe^{4+} respectively, where the valence of Fe is connected to $p(O_2)$ through the oxidation reactions (4) and (5).

$$V^{\bullet\bullet}_{O} + 2Fe'_{Fe} + \frac{1}{2}O_2(g) = 2Fe^{\times}_{Fe} + O^{\times}_{O} \quad (4)$$

$$V^{\bullet\bullet}_{O} + 2Fe^{\times}_{Fe} + \frac{1}{2}O_2(g) = 2Fe^{\bullet}_{Fe} + O^{\times}_{O} \quad (5)$$

The total electrical conductivity (σ_{tot}) of the material is described by eqn (6)

$$\sigma_{tot} = \sigma_{ion} + \sigma_e + \sigma_h \approx ne\mu_e + pe\mu_h \quad (6)$$

where σ_{ion} is the ionic conductivity, σ_e and σ_h are the contributions from electrons and holes, respectively, e is the charge of an electron, and μ_e and μ_h are the mobilities of electrons and holes respectively. For further calculations it is assumed that $\sigma_{ion} \ll \sigma_e, \sigma_h$. At the $p(O_2)$ corresponding to the minimum in the (σ_{min}) see Fig. 2a and b, the contribution from electrons and holes can be expressed by eqn (7)

$$\frac{\sigma_{min}}{2} = \sigma_h(\sigma_{min}) = \sigma_e(\sigma_{min}) = \left(K'_i\right)^{0.5} \quad (7)$$

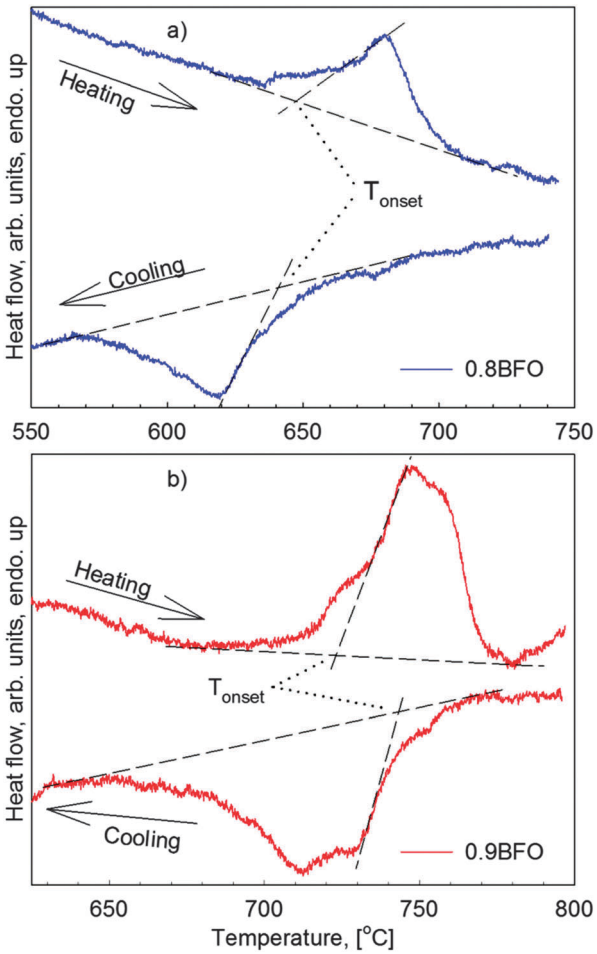

Fig. 7 DTA heat flow signal for 0.8BFO (a) and 0.9BFO (b). The black lines give the determination of T_{onset}.

where $K'_i = \sigma_e \cdot \sigma_h$. A combination of eqn (6) and (7) allows for determining $\sigma_h(p(O_2))$ and $\sigma_e(p(O_2))$. Following this, eqn (6) can be used to determine n and p. The mobility of electrons and holes (Table 2) was adjusted to fit the model, based on the corresponding data reported for $LaFeO_3$.[23]

Accurate data on the extent of A-site cation deficiency due to evaporation of Bi_2O_3 (and/or K_2O) during solid state reaction and sintering have so far not been determined, but accurate data on the cation non-stoichiometry are critical for further development of the model. Here, an assumption that $V'''_{Bi} = 0.01$ was introduced based on preliminary data.[46]

The optimized enthalpies for reactions (4) and (5) are listed in Table 2. The Gibbs energy was estimated by assuming that the entropy of the reactions is equal to -130 kJ mol^{-1} as argued by Bakken *et al.*[47]

The model for the conductivity, shown by the dashed lines in Fig. 2, shows that the dominating charge carriers in 0.8BFO and 0.9BFO are electrons or holes. While a positive Seebeck coefficient was measured in oxygen and air, a negative value was measured at low $p(O_2)$ proving the change of the sign of the main charge carrier (Fig. 3). The decreasing Seebeck coefficient with increasing temperature in oxygen and air can be rationalized

Table 2 Mobility of electrons and holes respectively used in the point defect model, and thermodynamic data for the point defect reactions for 0.8BFO and 0.9BFO

	Temperature [°C]	μ_e [cm^2 V^{-1} s^{-1}]	μ_h [cm^2 V^{-1} s^{-1}]	$\Delta_r H$ (eqn (4)) [kJ mol^{-1}]	$\Delta_r S$ (eqn (4)) [J mol^{-1}]	$\Delta_r G$ (eqn (4)) [kJ mol^{-1}]	$\Delta_r H$ (eqn (5)) [kJ mol^{-1}]	$\Delta_r S$ (eqn (5)) [J mol^{-1}]	$\Delta_r G$ (eqn (5)) [kJ mol^{-1}]
0.8BFO	700	0.052	0.050	−343	−130	−216	−28	−130	99
	750	0.054	0.074			−210			105
	800	0.056	0.107			−203			112
0.9BFO	700	0.046	0.030	−340	−130	−213	−31	−130	96
	750	0.047	0.063			−207			102
	800	0.056	0.107			−200			109

by a conventional semiconductor behaviour related to the number of charge carriers. The apparent increase of the Seebeck coefficient with temperature at low $p(O_2)$ is not fully understood. The importance of $V_O^{\bullet\bullet}$ in these BFO-rich materials is confirmed by the $p(O_2)$ dependence of the conductivity and the Seebeck coefficient. It is proposed that $V_{Bi}^{'''}$ is also an important point defect, but further work must be carried out to quantify the concentration of the cation vacancies.

The behaviour of the conductivity shown in Fig. 2 illustrates that the sintering atmosphere during fabrication of the ceramics is important for the conductivity, which falls in line with previous reports showing that conductivity can be reduced significantly by annealing in an inert or reducing atmosphere.[21] Although the results presented herein are on BKT substituted BFO, we propose that the present observations give valuable insight into the thermal evolution of the electrical conductivity of bulk pure BFO.[22–25]

The ferroelectric phase transition temperatures of 0.8BFO and 0.9BFO were determined by three different methods in reasonable agreement. The Curie temperature decreases upon decreasing BFO content in $(1-x)$BFO–xBKT as shown in Fig. 8. T_C values for 0.8BFO and 0.9BFO are still high making these materials interesting for high temperature applications. T_C is at the level of pure BKT for $x > \sim 0.4$, where a relaxor-type behaviour has been reported for pseudo cubic $(1-x)$BFO–xBKT solid solutions.[17,21]

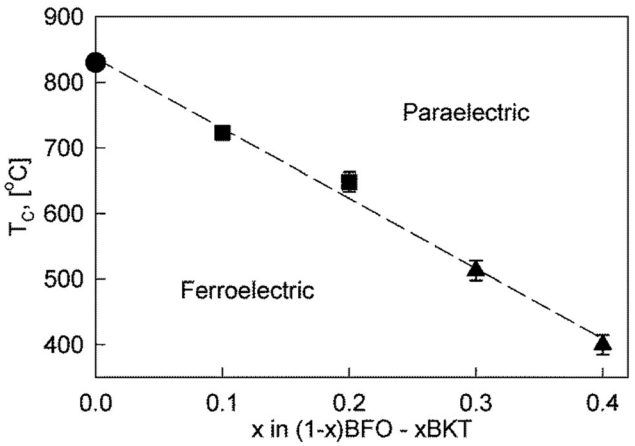

Fig. 8 The Curie temperature as a function of BFO-content in $(1-x)$BFO–xBKT. Squares from this work (DTA), circles[7] and triangles[21] from elsewhere. Dashed line is a guide to the eye.

The relaxation time for the redox driven point defect equilibria can be qualitatively derived from the DC conductivity and thermopower measurements although this was not the primary goal of the experiments. The electrical relaxation for 0.9BFO at 700 °C is shown in Fig. 9a where the normalized conductivity upon switching between O_2 and synthetic air are given as a function of time.

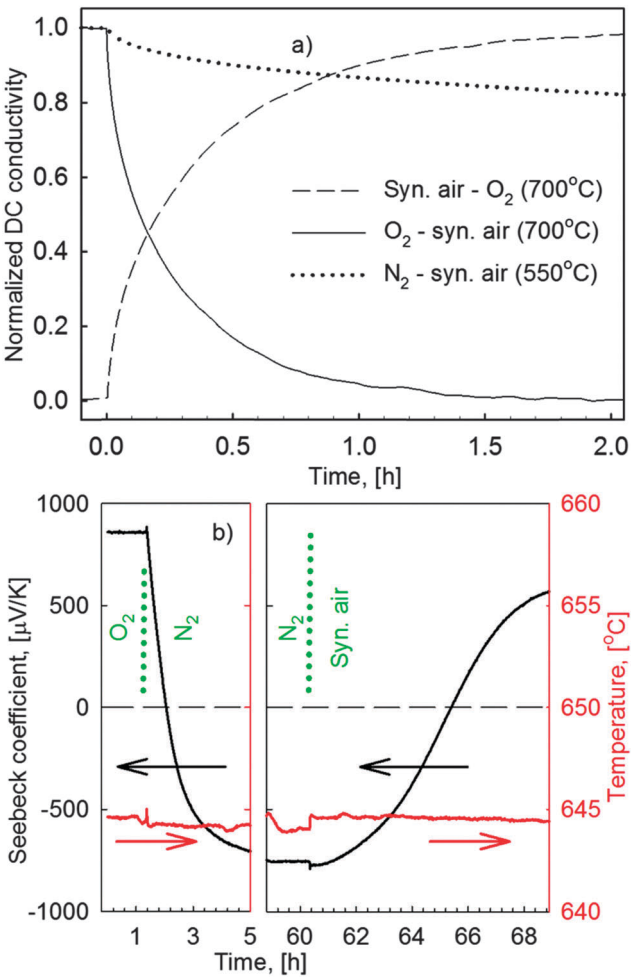

Fig. 9 (a) The relaxation of normalized conductivity upon switching between O_2 and synthetic air at 700 °C for 0.9BFO. Also shown is relaxation upon a shift from N_2 to synthetic air at 550 °C. (b) The material response for the Seebeck coefficient upon switching atmospheres from O_2 *via* N_2 to synthetic air at 650 °C (0.9BFO).

The relaxation time for oxidation and reduction was found to be comparable. Relaxation is an activated process and the relaxation time increases significantly with decreasing temperatures as illustrated by the relaxation curve at 550 °C, also depicted in Fig. 9a. The rapidly increasing relaxation time with decreasing temperature is in good agreement with similar data reported for 0.7BFO–0.3BKT by Morozov *et al.*[20] An important observation is the immediate response from the material to a shift in the atmosphere, even at 550 °C, implying a significant mobility of point defects at temperatures significantly below T_C. Fast relaxation was also observed during measurements of the Seebeck coefficient (Fig. 9b). The figure shows the reversible response going from p-type (in O_2) *via* n-type (in N_2) and back to p-type (in synthetic air) semiconductor behaviour.

The hardness of ferroelectric PZT can be tuned by acceptor and donor substitution,[48,49] and the hardening of acceptor substituted PZT has been explained by defect ordering due to rearrangement of oxygen vacancies.[50] Such ordering has also been studied in *e.g.* $BaTiO_3$ by long term aging at elevated temperatures ($<T_C$).[51] The driving force for point defect ordering and the formation of ''defect dipoles'' is minimization of electrostatic and probably also elastic energy that arises below T_C. Above T_C the material will have a paraelectric centrosymmetric structure with no driving force for ordering of charged point defects. Below T_C, a spontaneous polarization develops and the point defects will energetically prefer specific sites and form *i.e.* defect dipoles. These ordered defects subsequently act as effective pining centres for domain wall movement.[51] The hard ferroelectric characteristics of BFO have been related to point defects, though the mechanism is not yet clear.[4] Because the T_C of BFO is 830 °C, the driving force for point defect ordering will emerge already at high temperatures ($<T_C$). It is evident from the electrical relaxation curves shown in Fig. 9a that there is a significant oxygen ion mobility at temperatures as low as 550 °C. Since these measurements were performed on bulk materials, the diffusion length scale of the process involving a shift in the conductivity is on an mm scale.[52] The length scale of oxygen vacancy diffusion required for defect dipole formation is only within a unit cell. It is therefore reasonable to assume that oxygen vacancy mobility is sufficient at temperatures much lower than 550 °C. This is important because defect ordering in high T_C materials will start immediately below T_C if the point defects are sufficiently mobile. The high T_C of these materials and the mobility, evidenced by the relaxation data, show that point defect ordering likely occurs in BFO materials, possibly explaining the hard ferroelectric properties reported for these materials.[4]

The unit cell volume of $(1 - x)$BFO–xBKT decreases with the addition of BKT, along with a decrease in lattice distortion (c_{pc}/a_{pc}, Fig. 6). The lattice distortions of 1.0BFO,[45] 0.9BFO and 0.8BFO are ~1.015, 1.013 and 1.009, respectively. The large intrinsic lattice distortion (strain) observed for 1.0BFO is one factor contributing to the large piezoelectric response observed. The large strain in BFO may cause problems in the electromechanical performance. The introduction of BKT not only reduces the challenges to secondary phases during synthesis but do also offer the possibility of adjusting T_C as well as the crystallographic strain. $(1 - x)$BFO–xBKT becomes pseudo cubic $x > \sim 0.4$ which implies that most of the lattice distortion is suppressed by substitution, hence a low BKT content is preferable.[17] On the other hand, a low polarization and strain response to an applied electric field was observed for $x < \sim 0.4$. This reflects the hard ferroelectric characteristics of BFO making a wider range of applications of BFO as a piezoelectric or ferroelectric material challenging.[10] The understanding of the point defect chemistry presented herein offers a path to understand both hardening of BFO as well as reduction of the electrical conductivity and thereby the dielectric loss.

Finally, we address the relation of the major charge carriers and charged domain walls in BFO.[4,53,54] The conductivity along 71° domain walls has been described as n-type[54] (La-substituted BFO) and the concentration of oxygen vacancies has been shown to influence the domain wall conductivity[53] (pure BFO). The work described herein shows that both p- and n-type behaviour and electrical conductivity can be easily changed by annealing at different partial pressures of oxygen. The point defect equilibria, controlling the valence of Fe, can also be influenced by strain as recently shown for $CaMnO_{3-\delta}$.[55] The thermal processing of BFO, also in the case of BFO thin films, may therefore strongly affect the electrical properties.

5. Conclusions

Minima in the DC electrical conductivity of 0.8BFO and 0.9BFO were observed as a function of $p(O_2)$, which reflects a shift from p-type to n-type conductivity upon decreasing the partial pressure of oxygen. The change in the majority charge carrier was confirmed by the change in the sign of the Seebeck coefficient measured at different atmospheres. The conductivity was successfully described by a conventional mass action type point defect model by using electrons and holes as major charge carriers and oxygen vacancies and A-site vacancies as additional point defects. A high Curie temperature of BFO was retained with the introduction of 10 and 20 mol% BKT, and the ferroelectric to the paraelectric phase was established by a combination of dielectric spectroscopy thermal analysis and high temperature XRD.

Acknowledgements

The Research Council of Norway (FRINATEK project no. 197497/F20) is acknowledged for financial support. We acknowledge discussion concerning the interpretation of the data with Dr Maxim Morozov.

Notes and references

1 European Parliament, *Off. J. Eur. Union*, 2011, **54**(L174), 89.
2 J. Rödel, W. Jo, K. T. P. Seifert, E. M. Anton, T. Granzow and D. Damjanovic, *J. Am. Ceram. Soc.*, 2009, **92**, 1153.
3 G. Catalan and J. F. Scott, *Adv. Mater.*, 2009, **21**, 2463.

4 T. Rojac, A. Bencan, B. Malic, G. Tutuncu, J. L. Jones, J. E. Daniels and D. Damjanovic, *J. Am. Ceram. Soc.*, 2014, **97**, 1993.
5 T. Rojac, M. Kosec and D. Damjanovic, *J. Am. Ceram. Soc.*, 2011, **94**, 4108.
6 D. Lebeugle, D. Colson, A. Forget and M. Viret, *Appl. Phys. Lett.*, 2007, **91**, 022907.
7 R. Palai, R. S. Katiyar, H. Schmid, P. Tissot, S. J. Clark, J. Robertson, S. A. T. Redfern, G. Catalan and J. F. Scott, *Phys. Rev. B: Condens. Matter Mater. Phys.*, 2008, **77**, 014110.
8 S. Selbach, M.-A. Einarsrud and T. Grande, *Chem. Mater.*, 2009, **21**, 169.
9 M. Valant, A. K. Axelsson and N. Alford, *Chem. Mater.*, 2007, **19**, 5431.
10 T. Rojac, M. Kosec, B. Budic, N. Setter and D. Damjanovic, *J. Appl. Phys.*, 2010, **108**, 074107.
11 Y. Hiruma, H. Nagata and T. Takenaka, *Jpn. J. Appl. Phys.*, 2007, **46**, 1081.
12 C. F. Buhrer, *J. Chem. Phys.*, 1962, **36**, 798.
13 Y. Hiruma, R. Aoyagi, H. Nagata and T. Takenaka, *Jpn. J. Appl. Phys.*, 2005, **44**, 5040.
14 E. T. Wefring, M. I. Morozov, M.-A. Einarsrud and T. Grande, *J. Am. Ceram. Soc.*, 2014, **97**, 2928.
15 J. Bennett, A. J. Bell, T. J. Stevenson, R. I. Smith, I. Sterianou, I. M. Reaney and T. P. Comyn, *Mater. Lett.*, 2013, **94**, 172.
16 M. I. Morozov, M.-A. Einarsrud, T. Grande and D. Damjanovic, *Ferroelectrics*, 2012, **439**, 88.
17 M. I. Morozov, M.-A. Einarsrud and T. Grande, *Appl. Phys. Lett.*, 2012, **101**, 252904.
18 H. Matsuo, Y. Noguchi, M. Miyayama, M. Suzuki, A. Watanabe, S. Sasabe, T. Ozaki, S. Mori, S. Torii and T. Kamiyama, *J. Appl. Phys.*, 2010, **108**, 104103.
19 J. M. Kim, Y. S. Sung, J. H. Cho, J. K. Song, M. H. Kim, H. H. Chong, T. G. Park, D. Do and S. S. Kim, *Ferroelectrics*, 2010, **404**, 88.
20 M. I. Morozov, M.-A. Einarsrud and T. Grande, *Appl. Phys. Lett.*, 2014, **104**, 122905.
21 M. I. Morozov, M.-A. Einarsrud and T. Grande, *J. Appl. Phys.*, 2014, **115**, 044104.
22 T. R. Paudel, S. S. Jaswal and E. Y. Tsymbal, *Phys. Rev. B: Condens. Matter Mater. Phys.*, 2012, **85**, 104409.
23 A. S. Poghossian, H. V. Abovian, P. B. Avakian, S. H. Mkrtchian and V. M. Haroutunian, *Sens. Actuators, B*, 1991, **4**, 545.
24 Z. Dai and Y. J. Akishige, *J. Phys. D: Appl. Phys.*, 2010, **43**, 445403.
25 Z. Zhang, P. Wu, L. Chen and J. L. Wang, *Appl. Phys. Lett.*, 2010, **96**, 232906.
26 N. Masó and A. R. West, *Chem. Mater.*, 2012, **24**, 2127.
27 K. Kalantari, I. Sterianou, S. Karimi, M. C. Ferrarelli, S. Miao, D. C. Sinclair and I. M. Reaney, *Adv. Funct. Mater.*, 2011, **21**, 3737.
28 X. D. Qi, J. Dho, R. Tomov, M. G. Blamire and J. L. MacManus-Driscoll, *Appl. Phys. Lett.*, 2005, **86**, 062903.
29 K. Abe, N. Sakai, J. Takahashi, H. Itoh, N. Adachi and T. Ota, *Jpn. J. Appl. Phys.*, 2010, **49**, 09MB01.
30 Y. Wang and C.-W. Nan, *Appl. Phys. Lett.*, 2006, **89**, 052903.
31 M. C. Li and J. L. MacManus-Driscoll, *Appl. Phys. Lett.*, 2005, **87**, 252510.
32 S. Hunpratub, P. Thongbai, T. Yamwong, R. Yimnirun and S. Maensiri, *Appl. Phys. Lett.*, 2009, **94**, 062904.
33 V. L. Kozhevnikov, I. A. Leonidov, M. V. Patrakeev, E. B. Mitberg and K. R. Poeppelmeier, *J. Solid State Chem.*, 2001, **158**, 320.
34 J. Mizusaki, M. Yoshihiro, S. Yamauchi and K. Fueki, *J. Solid State Chem.*, 1985, **58**, 257.
35 J. Mizusaki, T. Sasamoto, W. R. Cannon and H. K. Bowen, *J. Am. Ceram. Soc.*, 1982, **65**, 363.
36 T. Arakawa, S. Tsuchi-ya and J. Shiokawa, *Mater. Res. Bull.*, 1981, **16**, 97.
37 M. Siemons, A. Leifert and U. Simon, *Adv. Funct. Mater.*, 2007, **17**, 2189.
38 I. Wærnhus, P. E. Vullum, R. Holmestad, T. Grande and K. Wiik, *Solid State Ionics*, 2005, **176**, 2783.
39 A. A. Coelho, *TOPAS Academic: General Profile and Structure Analysis Software for Powder Diffraction Data*, Bruker AXS, Karlsruhe, Germany, 2004.
40 S. M. Selbach, T. Tybell, M. A. Einarsrud and T. Grande, *Phys. Rev. B: Condens. Matter Mater. Phys.*, 2009, **79**, 214113.
41 S. M. Selbach, T. Tybell, M.-A. Einarsrud and T. Grande, *Chem. Mater.*, 2009, **21**, 5176.
42 P. V. B. Rao, E. V. Ramana and T. B. Sankaram, *J. Alloys Compd.*, 2009, **467**, 293.
43 T. Yokota, R. Aoyagi and M. Gomi, *J. Ceram. Soc. Jpn.*, 2013, **121**, 675.
44 D. C. Arnold, K. S. Knight, G. Catalan, S. A. T. Redfern, J. F. Scott, P. Lightfoot and F. D. Morrison, *Adv. Funct. Mater.*, 2010, **20**, 2116.
45 S. M. Selbach, T. Tybell, M.-A. Einarsrud and T. Grande, *Adv. Mater.*, 2008, **20**, 3692.
46 M. Christensen, Master thesis, Norwegian University of Science and Technology, Trondheim, Norway, 2013.
47 E. Bakken, T. Norby and S. Stølen, *J. Mater. Chem.*, 2002, **12**, 317.
48 M. I. Morozov and D. Damjanovic, *J. Appl. Phys.*, 2008, **104**, 034107.
49 M. I. Morozov and D. Damjanovic, *J. Appl. Phys.*, 2010, **107**, 034106.
50 A. Chandrasekaran, D. Damjanovic, N. Setter and N. Marzari, *Phys. Rev. B: Condens. Matter Mater. Phys.*, 2013, **88**, 214116.
51 X. B. Ren, *Nat. Mater.*, 2004, **3**, 91.
52 T. Grande, J. R. Tolchard and S. M. Selbach, *Chem. Mater.*, 2012, **24**, 338.
53 J. Seidel, P. Maksymovych, Y. Batra, A. Katan, S. Y. Yang, Q. He, A. P. Baddorf, S. V. Kalinin, C. H. Yang, J. C. Yang, Y. H. Chu, E. K. H. Salje, H. Wormeester, M. Salmeron and R. Ramesh, *Phys. Rev. Lett.*, 2010, **105**, 197603.
54 S. Farokhipoor and B. Noheda, *Phys. Rev. Lett.*, 2011, **107**, 127601.
55 U. Aschauer, R. Pfenninger, S. M. Selbach, T. Grande and N. A. Spaldin, *Phys. Rev. B: Condens. Matter Mater. Phys.*, 2013, **88**, 054111.